New ultra-high temperature nanoindentation system for operating at up to 1100 °C

Minnert, Christian; Oliver, Warren C.; Durst, Karsten

(2020)

Materials and Design 192 (2020) 108727

Contents lists available at ScienceDirect

Materials and Design

journal homepage: www.elsevier.com/locate/matdes

New ultra-high temperature nanoindentation system for operating at up to 1100 °C

Christian Minnert [a,*], Warren C. Oliver [b], Karsten Durst [a]

[a] Physical Metallurgy, Materials Science Department, Technical University of Darmstadt, Germany
[b] Nanomechanics Inc./KLA, Oak Ridge, TN, USA

HIGHLIGHTS

- A new high-temperature and in-situ nanoindentation system was developed for testing temperature of up to 1100 °C.
- The sophisticated temperature management with tip and sample heating as well as actuator cooling leads to low drift rates.
- The determination of reliable hardness and Young's modulus data was presented by constant strain rate tests on fused silica for $T < 300$ °C and Mo for testing up to 1100 °C.
- The applicability of the system to determine the creep behavior has been shown for single crystalline Ni up to 1100 °C was by using indentation strain rate jump and step load and hold methods.

GRAPHICAL ABSTRACT

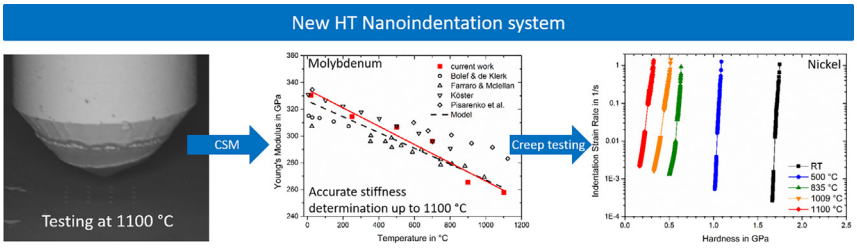

ARTICLE INFO

Article history:
Received 19 December 2019
Received in revised form 26 March 2020
Accepted 9 April 2020
Available online 13 April 2020

Keywords:
High-temperature nanoindentation
Creep
Strain rate sensitivity
Hardness
Young's modulus

ABSTRACT

In this work a new ultra-high temperature (UHT) nanoindentation system for testing at up to 1100 °C is presented. The system is capable to perform indents from small scale up to large indentation depths due to the combination of a 1 N actuator and a frame stiffness of $>1 \cdot 10^6\ {}^{N}/_{m}$ even at 1100 °C. Dynamic testing allows a continuous determination of the contact stiffness (CSM) and thus also the depth-dependent hardness and indentation modulus. Low drift rates can be achieved by an independent tip and sample heating. Operating the nanoindenter inside a scanning electron microscope (SEM) equipped with a high temperature backscattered electron (BSE) detector opens the possibility of in-situ observations, as high vacuum minimizes oxidation effects. The HT capability of the system is demonstrated on three reference materials: fused silica, molybdenum assessing the change in modulus with increasing temperature using constant strain rate tests (CSR). The creep response of single crystalline Ni has been assessed by strain rate jump (SRJ) as well as a step-load and hold creep (SLH) method. The resulting modulus, hardness as well as the strain rate sensitivity from RT up to 1100 °C are in good accordance with literature data, highlighting the applicability of the system.

* Corresponding author.
E-mail address: c.minnert@phm.tu-darmstadt.de (C. Minnert).

https://doi.org/10.1016/j.matdes.2020.108727

1. Introduction

Over the past decades, the continuous development of new nanoindentation systems and new test protocols has made nanoindentation testing to a powerful tool for mechanical characterization on small length scales [1,2]. The advantages compared to conventional, macroscopic tests are not only the simple sample preparation and the rapid test rates, but also the variety of characterization options. Nanoindenters are used to determine hardness and Young's modulus on a local length scale. Furthermore, strain rate dependencies, fracture toughness, creep, fatigue behavior or adhesive strength of layers and coatings can be determined [3–7].

In order to increase the efficiency of jet engines or gas turbines for power generation, their operating or combustion temperature must be increased. However, this is often limited by the materials used [8]. Therefore, the development of new high temperature (HT) materials, such as Ni or Co-based alloys, as well as the improvement of thermal barrier coatings and bond coats, plays an important role in current research [8–14].

For this reason, nanoindentation systems have been developed for testing the local properties of materials and thin coatings at elevated temperatures [1]. Nanoindentation thereby enables to characterize the influence of alloying elements, chemical or microstructural gradients on a single phase of a material [15–17].

Thermal activated mechanisms can be analyzed by nanoindentation testing in terms of strain rate sensitivities/stress exponents, activation volumes and activation energies [3,5,14,18–22]. Therefore, tests with a controlled strain rate at different temperature or a changing strain rate have to be carried out. It has been shown that local, nanoindentation experiments, introducing a complex stress state in the material, provide comparable results to macroscopic, bulk and/or uniaxial experiments [3,5,19–21,23–26].

However, nanoindentation testing at elevated temperatures is quite challenging and several issues need to be considered [1]. Chemical reactions between tip and sample can lead to high tip wear, which strongly affects the measurements especially at low indentation depths [27]. In addition, a sophisticated temperature management is necessary to keep the drift rates as low as possible. Thermal drift can be caused by a temperature mismatch between tip and sample, therefore an independent sample and tip heating is required in order to match the temperatures [1]. Dynamic testing enables the possibility to measure the stiffness and, thus, the Young's modulus continuously. The stiffness data can also be used to calculate the hardness [5]. Environment assisted HT nanoindentation testing can be used to determine mechanical properties of e.g. superalloys under more application-related conditions where oxidation plays a role [28–30]. However, the oxidation of a material makes it more difficult to determine reliable material properties during nanoindentation. For this reason, experiments at high temperatures are preferably carried out in vacuum to minimize the influence of oxidation effects. The formation of thin oxide layers during heating cannot be completely avoided even in a high vacuum, but it can be significantly reduced [1,31–33].

The maximum reported testing temperature of the current HT nanoindentation systems is 1000 °C working in vacuum [32]. However, the determination of the contact stiffness data at these extreme temperatures is challenging due to high drift rates and insufficiently fast unloading rates [32].

In this work, nanoindentation tests from room temperature (RT) to 1100 °C were performed using an advanced commercial prototype, load-controlled in-situ system from Nanomechanics Inc./KLA. The ultra-high operating temperature of the system offers the possibility to determine mechanical properties as well as thermally activated processes of HT materials at their application temperature. Operating the nanoindenter inside a scanning electron microscope (SEM) equipped with a HT backscattered electron (BSE) detector opens the possibility of in-situ observations, as high vacuum reduces oxidation effects [32,34].

The testing capabilities of the new system is demonstrated on three different materials using the continuous stiffness measurement (CSM) method, strain rate jump (SRJ) tests and step load and the hold (SLH) creep method. The low T capabilities is shown on fused silica as a reference material for indentation testing. The high temperature tests were performed on polycrystalline body centered cubic molybdenum, for which temperature dependent modulus data is available. Single crystalline (SX) Ni with its face centered cubic structure is an important base metal for many high temperature materials as Ni-base superalloys and has been chosen as a reference for the creep tests.

1.1. Dynamic indentation testing for continuous property determination and measurement of thermally activated processes

Nanoindentation enables the determination of thermally activated mechanisms, by using different loading scenarios [3,5,18–21]. The following subsection gives a brief overview of the various nanoindentation test methods using a pyramid-shaped Berkovich indenter and their comparison to macroscopic, uniaxial tests.

Indentation testing relies on an accurate determination of the contact area A_C, which is based on Sneddon's equation, relating the contact stiffness S to the reduced modulus E_R and the contact area. The definition of S is shown in Eq. (1) [35,36]:

$$S = \frac{2\beta}{\sqrt{\pi}} \cdot E_R \cdot \sqrt{A_c} = S_{CSM} \tag{1}$$

with the constant β and the unloading stiffness S_{CSM} determined by a dynamic oscillating loading signal.

Thus, the contact area can be expressed as:

$$A_c = \frac{\pi}{4\beta^2} \cdot \frac{S^2}{E_R^2}. \tag{2}$$

The correct contact depth h_c can now be calculated by knowing the correct tip area function $f(h_c) = A_c$:

$$f(h_c) = m_0 h_c^2 + m_1 h_c + m_2 h_c^{1/2} + m_3 h_c^{1/4} + \ldots + m_n h_c^{2^{1-n}} = \sum_{i=0}^{n} m_i h_c^{2^{1-i}} \tag{3}$$

determined by calibration on a reference material like fused silica [36]. It has been discussed in literature that the hardness based on stiffness gives much more reliable hardness data, since it is unaffected by thermal drift, pile-up and sink-in [5].

The three different test methods used in this work are presented below. Further details on the used input parameters are given in subsection 3.1.

A constant strain rate $\dot{\varepsilon}$ is used in the continuous stiffness measurement (CSM) method, where the loading signal is superimposed by a sinusoidal oscillation. The definition of the strain rate, based on the work of Mayo and Nix [37], is given in Eq. (4) [5,38,39].

$$\dot{\varepsilon} = \frac{\dot{h}}{h} = \frac{1}{2}\left(\frac{\dot{P}}{P} - \frac{\dot{H}}{H}\right) \approx \frac{\dot{S}}{S} \approx \frac{1}{2}\frac{\dot{P}}{P} \tag{4}$$

with indentation depth h, applied load P and hardness H. The stiffness signal S can be determined continuously. Thus, it is possible to calculate the hardness and Young's modulus as a function of indentation depth. The hardness is defined by the ratio of the applied load and depth dependent projected contact area [5,38]:

$$H = \frac{P}{A_c} = \frac{P \cdot 4\beta^2 \cdot E_R^2}{\pi \cdot S^2} \tag{5}$$

with the reduced modulus E_R and the constant β. The Young's modulus E of the sample can be calculated with Eq. (6) [38]:

$$E_{sample} = \frac{(1-\nu^2)_{sample}}{\frac{1}{E_r} - \left(\frac{1-\nu^2}{E}\right)_{indenter}} \tag{6}$$

assuming a known modulus of the indenter material, as well as the Poisson's ratio ν of the tip and sample material.

The SRJ method, developed by Maier et al. [3], is based on the CSM method mentioned above. In contrast to a CSM test is the strain rate changed within a single test (see Fig. 1). This allows to determine the strain rate sensitivity m in a "constant" volume/microstructure element. The strain rate sensitivity m of a material can be computed by comparing the strain rate dependent hardness values of the material:

$$m = \frac{1}{n} = \frac{d(\ln H)}{d(\ln \varepsilon)} \tag{7}$$

with n being the stress exponent.

The correct analysis of strain rate dependencies of soft materials or at high temperatures can be rather difficult as the hardness changes only slightly with strain rate. The analysis becomes easier if the applied strain rate can be varied over several orders of magnitude. However, this is typically limited by about three orders of magnitude (e.g. $\varepsilon = 10^{-1} - 10^{-41}/_{s}$) with the SRJ method described above [18,26,40]. Therefore, the load and hold creep tests with an initial step load (SLH) according to Sudharshan Phani et al. [21,41] were performed (see Fig. 1) on single crystalline nickel. The big advantage of the SLH test is, that the strain rate can be varied by seven orders of magnitude within a single test [41]. Furthermore, the test duration is only 40 s, reducing the tip and sample interaction as well as thermal drift effects.

The test SLH protocol consists of two different test segments. In the first segment, the tip is slowly approaching the sample surface (no impact) and after contact, a step load is applied with a defined loading rate which results in very high strain rates in the beginning of the experiment. Afterwards, the load is kept constant for a short time e.g. 1.5 s, while the hardness is calculated by the applied load and the projected contact area, the strain rate is determined by $\dot{h}/_{h}$.

After 1.5 s the dynamics/sinusoidal oscillation was switched on. This marks the start of the second test segment, which is similar to a standard CSM test. Also here the load is kept constant, the strain rate is described by $\dot{S}/_{S}$. Thermal drift is a big issue in indentation creep testing, therefore the stiffness based hardness was calculated in this test segment (Eq. (5)).

Hardness and strain rate determined by indentation testing has to be converted into uniaxial stress σ and strain rate ε using Eqs. (8) and (9) [21,25] in order to compare the results with literature data determined by macroscopic testing:

$$\sigma = \left(\frac{1}{Fc^2}\right)\left(\frac{L}{\pi(h\ tan(\theta))^2}\right) \tag{8}$$

$$\varepsilon = \left(\frac{1}{c\tan\theta}\right)\left(\frac{1}{h}\right)\left(\frac{dh}{dt}\right) \tag{9}$$

with reduced contact pressure F, pile-up/sink-in parameter c, equivalent cone angle θ, Load L and indentation depth h. The activation energy for creep can be calculated with Eq. (10) [19]:

$$\frac{H}{E} = G \cdot \exp\left(\frac{Q_c}{nRT}\right) \tag{10}$$

with pre-exponential coefficient G, activation energy Q_c in kJ/mol, stress exponent n, gas constant R and absolute temperature T.

2. New high temperature indentation system

The newly developed ultra-high temperature nanoindentation system is equipped with an actively cooled high load actuator with a maximum load of 1 N. Thereby the system is able to perform indents from small scale all the way up to large indentation depths in order to minimize the impact of tip blunting and surface oxidation on the test results. The indenter was designed for high machine stiffness, which is necessary for accurate data analyzation at large indentation depths. The actuator can be driven at a high frequency, allowing a continuous determination of the contact stiffness. This is essential for determining the depth dependent material properties, like hardness and modulus. Furthermore, the contact stiffness can be used to determine pile-up and drift independent hardness values [5]. The active cooling of the actuator ensures that machine calibration during high temperature or long term testing remains constant and comparable to the RT properties. An accurate sample positioning is achieved by using a piezo-driven x-y stage (SmarAct GmbH) with a resolution of 20 nm.

The system is equipped with independent tip and sample heaters. K-type thermocouples are used to measure and control the temperature of the sample, tip and actuator housings. The temperature control is carried out via PID loops which allows an independently adjustment of

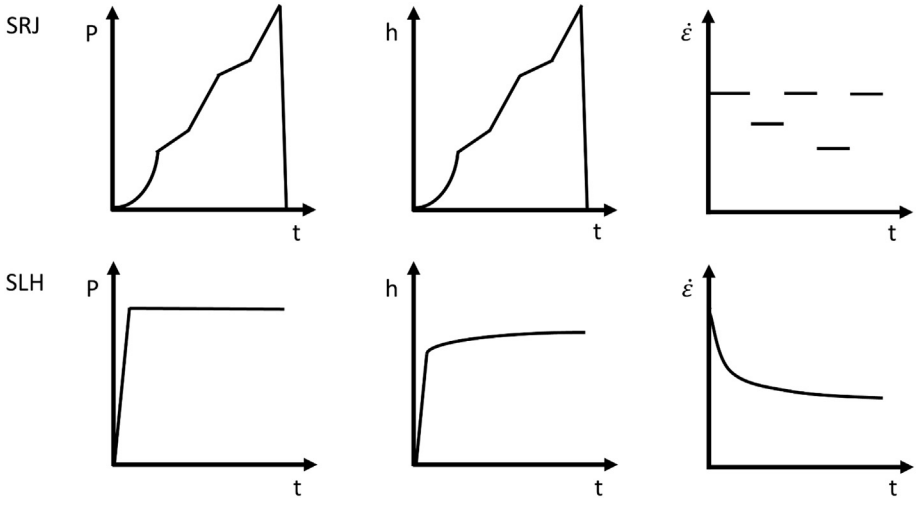

Fig. 1. Schematic illustration of the time dependent load, indentation depth and strain rate during SRJ and SLH tests.

the sample and tip temperature. Thus, low drift rates can be achieved after temperature matching between tip and sample. A detailed description of the system will be given in the subsequent sections.

2.1. Tip holder, shaft design and actuator

A schematic drawing of the indenter system is shown in Fig. 2. The centerpiece of the system is the 1 N actuator, the surrounding actuator housing can be actively cooled via a Peltier heat pump and the cool block on top of the housing. It is thermally insulated from the two Cu blocks on the side of the actuator housing. These lateral Cu blocks are connected with the base of the column via cooling springs. The temperature of these blocks is also controlled via Peltier elements located between the Cu blocks and the outer cooling blocks.

The magnetic driven and load controlled actuator is able to perform frequency specific loading experiments to determine the elastic stiffness of the sample continuously with a dynamic frequency of up to 1000 Hz. The maximum displacement range is 80 μm with a resolution of 0.04 nm and a noise floor below 0.1 nm. The load is applied with a load resolution of 6 nN, the load noise floor of the system is 0.9 μN. These specifications do not change while heating the system due to the active cooling of the actuator housing which keeps the actuator at room temperature. Thus, the optimal force and displacement resolution, as well as the low noise level will be maintained even at a temperature of 1100 °C (Appendix A.1). Active cooling also offers an advantage in long-term creep testing at RT, by continuously dissipating the heat generated in the actuator during holding periods.

A high frame stiffness is achieved by separating the resistive tip heater from the loading axis. This results in a frame stiffness higher than $1 \cdot 10^6 \, {}^{N}/_{m}$ even at maximum operation temperature.

2.2. Sample holder with integrated heating and cooling option

In contrast to standard RT systems, the specimen cannot be glued to the specimen holder as conventional adhesives cannot withstand these extreme temperatures. It is therefore clamped onto the sample heater using four 0.5 mm thick tungsten wires (see Fig. 2). Only a small amount of heat is transferred from the sample to the sample holder due to the small contact areas between the wires and the sample, reducing the required heating and cooling capacities. An additional molybdenum sheet is placed between the sample and sample heater to protect the heating element and prevents the sample from being welded to the heating element. A trench was etched into the molybdenum sheet in which the sample thermocouple can be placed. Alternatively, the sample thermocouple can be inserted directly into the sample using a lateral drill hole, if available. This offers the possibility to measure the sample temperature close to the sample surface.

2.3. Cooling system

Cooling is provided by a closed loop cooling system consisting of a high-pressure pump, a water chiller and Peltier heat pump elements. The water is first pumped with a pressure of about 586 kPa (5.86 bar) through the cooling block on the sample side and afterwards through the three cooling blocks on the actuator housing. The water cooled block on the sample side of the system is in direct contact with the copper block surrounding the sample heater. The temperature of that block is kept close to RT by varying the water temperature via the water chiller in the delivery system.

The heat from the indenter tip is extracted at the base of the column. This is accomplished through cooling springs that provide a thermal path from the base of the column to the cooling system. Two of the water cooled blocks on the actuator side of the system are attached to the end of the heat extraction springs via two Peltier heat pumps. These pumps are controlled so that the base of the column that attaches to the actuator shaft remains at RT. The additional mechanical stiffness due to the cooling springs is reduced by using multiple thin springs instead of two thick springs at the same thermal cross section. The final water cooled block on the actuator side of the system is attached to the copper block surrounding the actuator through an additional Peltier heat pump that is controlled to maintain the actuator at room temperature at all times. A nickel plated heat shield between the tip heater and the actuator housing reduce the heating of the actuator caused by radiation.

2.4. Temperature control and adjustment

Numerous publications are dealing with the cause and effect of thermal drift on indentation test results [1,33,42–45]. In order to reduce the influence of thermal drift a temperature adjustment between tip and sample has to be carried out before testing at elevated temperatures to achieve a thermal equilibrium. Changes in displacement signal are caused by thermal drift. Thermal drift can be caused by a temperature mismatch between tip and sample (contact drift) and/or by a change in temperature of the whole gantry (system drift). The adjustment of tip and sample temperature is done by using a standardized, semi-automated temperature matching procedure developed by Nanomechanics Inc./KLA. A

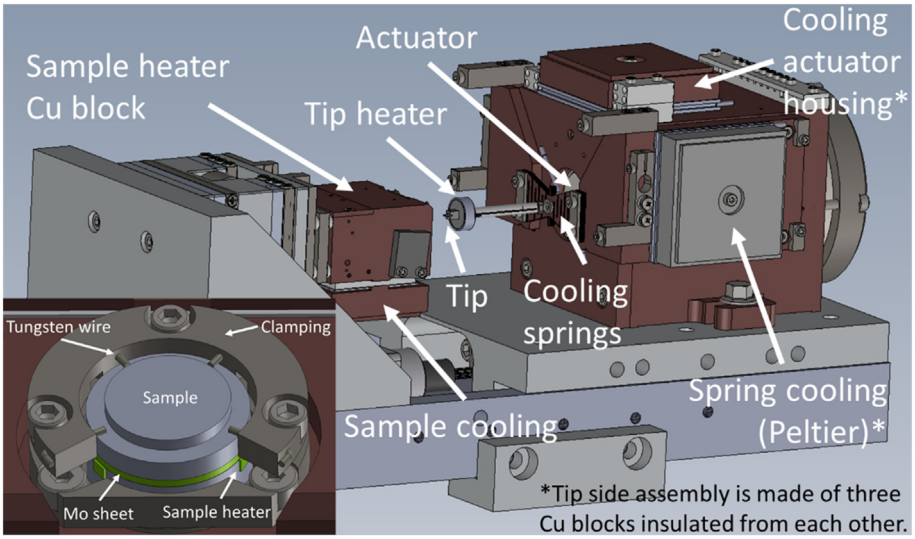

Fig. 2. Indenter set-up. The heat shield is not shown for illustration reasons.

detailed description of the temperature adjustment procedure is given in the Appendix A.2.

2.5. Test environment

The indenter is installed inside a Tescan Vega 3 scanning electron microscope (SEM) equipped with a secondary electron (SE) detector and a water cooled backscattered electron (BSE) detector. In-situ experiments, sample positioning and imaging even at the maximum operating temperature can be carried out using the integrated water-cooled BSE detector. Fig. 3 is taken with the water cooled backscattered electron detector at 1100 °C to demonstrate the imaging capability of the SEM at maximum operating temperature of 1100 °C. The high vacuum environment ($\sim 10^{-3} - 10^{-4}\ Pa$) reduces oxidation effects during testing. Low noise levels are achieved by an active vibration damping of the vacuum chamber.

3. Results and discussion

3.1. Testing of different materials for system validation

Nanoindentation experiments at elevated temperatures were performed using the continuous stiffness measurement (CSM) technique, strain rate jump (SRJ) and the step load and hold (SLH) test protocols. All tests were performed in batch mode. Fused silica was tested as it is widely used as a reference material due to its isotropic mechanical properties. Tip shape and frame stiffness calibration at room temperature were performed according to Oliver and Pharr [36]. Additional tests on fused silica were performed after testing at high temperatures in order to investigate changes in tip geometry. The results are presented in in the Appendix A.3.

For the CSM tests, a maximum load of 1 N and a constant input strain rate $\left(P/_P\right)$ of 0.2 1/s were applied, followed by a peak load hold time of 5 s and an unloading by 90% of P_{max}. The unloading has been performed in 1 s. Thermal drift was measured for 40 s after a settle time of 40 s at 0.1 P_{max}. For the superimposed CSM loading a target frequency of 100 Hz and a harmonic amplitude of 4 nm were used. SRJ tests were performed according to Maier et al. [3] with a change in strain rate $\left(P/_P\right)$ from 0.2 1/s to 0.05 1/s. Creep test with an initial step load were performed according to Sudharshan Phani et al. [21,41]. A step load of 95 mN was applied with a loading rate of 200 mN/s and hold constant for 1.5 s before switching on the dynamics (CSM) for 40 s.

Molybdenum was chosen as a reference material due to its high temperature mechanical properties which make it an interesting construction material for HT applications. The high thermal conductivity of Mo, compared to fused silica, causes higher drift rates if there is a temperature mismatch between tip and sample. An advantage compared to other materials is that Mo does not cause excessive tip wear due to chemical reactions with the sapphire tip used [27]. The sample thermocouple was placed into a lateral drill hole of the Mo sample. Thus, the temperature could be measured very close to the test locations.

Nickel is the base metal for a variety of high temperature alloys, the so called Ni-based superalloys and therefore an attractive material for future research. Furthermore, there is a good data set on the creep behavior, which can be used for comparison. The strain rate sensitivity of a Ni single crystal in ⟨100⟩ orientation was determined using SRJ and creep tests with an initial step load. Further information about the production and processing of the Ni single crystal can be found in [46,47].

3.2. 3.2 Fused silica

Constant strain rate tests were performed as stated above, using a standard Berkovich diamond tip (MicroStar). Fused silica was tested at room temperature, 200 °C and 300 °C. The sample temperature was the set value, while the tip temperature was adjusted to achieve an isothermal contact. Temperature matching was carried out with the semi-automatic procedure described in the Appendix A.2, using a maximum force of 30 mN and cycle load on/load off time of 30 s/90 s, until drift rates below 0.16 nm/s were achieved. The sample thermocouple was placed in the Mo sheet between sample and sample heater. A difference in tip and sample temperature of about 0.8 °C was determined during temperature matching at 200 °C.

The temperature change during testing was well below 0.01 °C (Fig. 4) which results in drift rates of 0.158 nm/s. The slight change in temperature at the end of the test segment is caused by a changing thermal contact between tip and sample due to partial unloading for thermal drift measurement. The measured temperature of the actuator was 22.5 °C respectively 23.8 °C during testing at 200 °C and 300 °C.

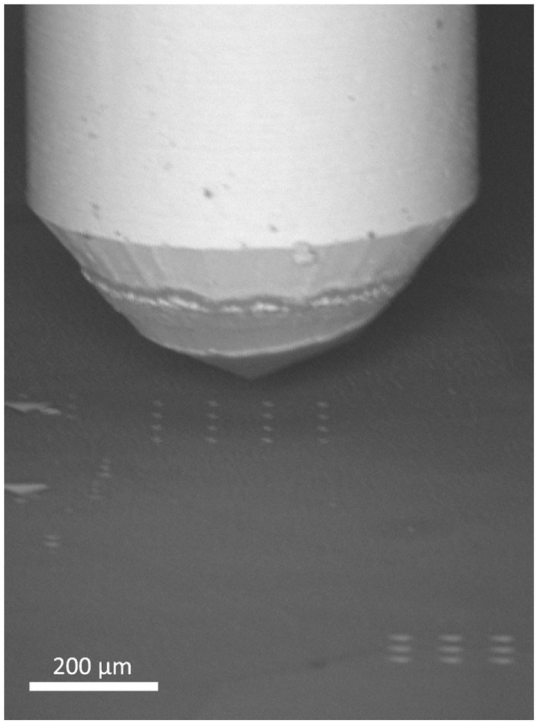

Fig. 3. Backscattered electron contrast image of a sapphire tip above a nickel sample at 1100 °C.

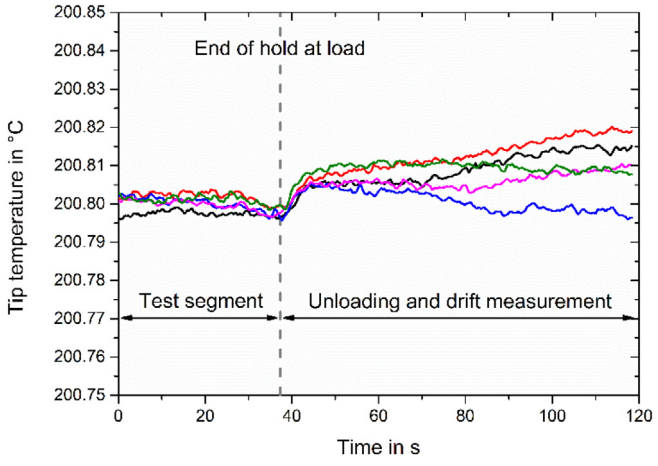

Fig. 4. Tip temperature during the indentation of fused silica at 200 °C. Temperatures are plotted for the test segment as well as the subsequent drift measurement segment.

The good temperature stability even at low temperatures like 200 °C demonstrates the capability of the system to control the heating power very well even at low current outputs.

The corresponding load-displacement data, as well as the dynamic contact stiffness are plotted in Fig. 5a and b. Hardness and modulus are shown in Fig. 5c and d. The indentation depth as well as the contact stiffness values are increasing with temperature. This leads to the well observed phenomena in literature, that the hardness of fused silica is decreasing with temperature, while at the same time the Young's modulus is slightly increasing [2,33,43,44,48,49].

The measured hardness and modulus data in this study fit very well with literature (Fig. 5e–f). Higher drift rates have only a minor effect on the data due to the large contact depths achieved by the high load applied. The changing system stiffness during heating was compensated in order to get a depth independent, constant modulus of the sample. The frame stiffness is slightly decreasing

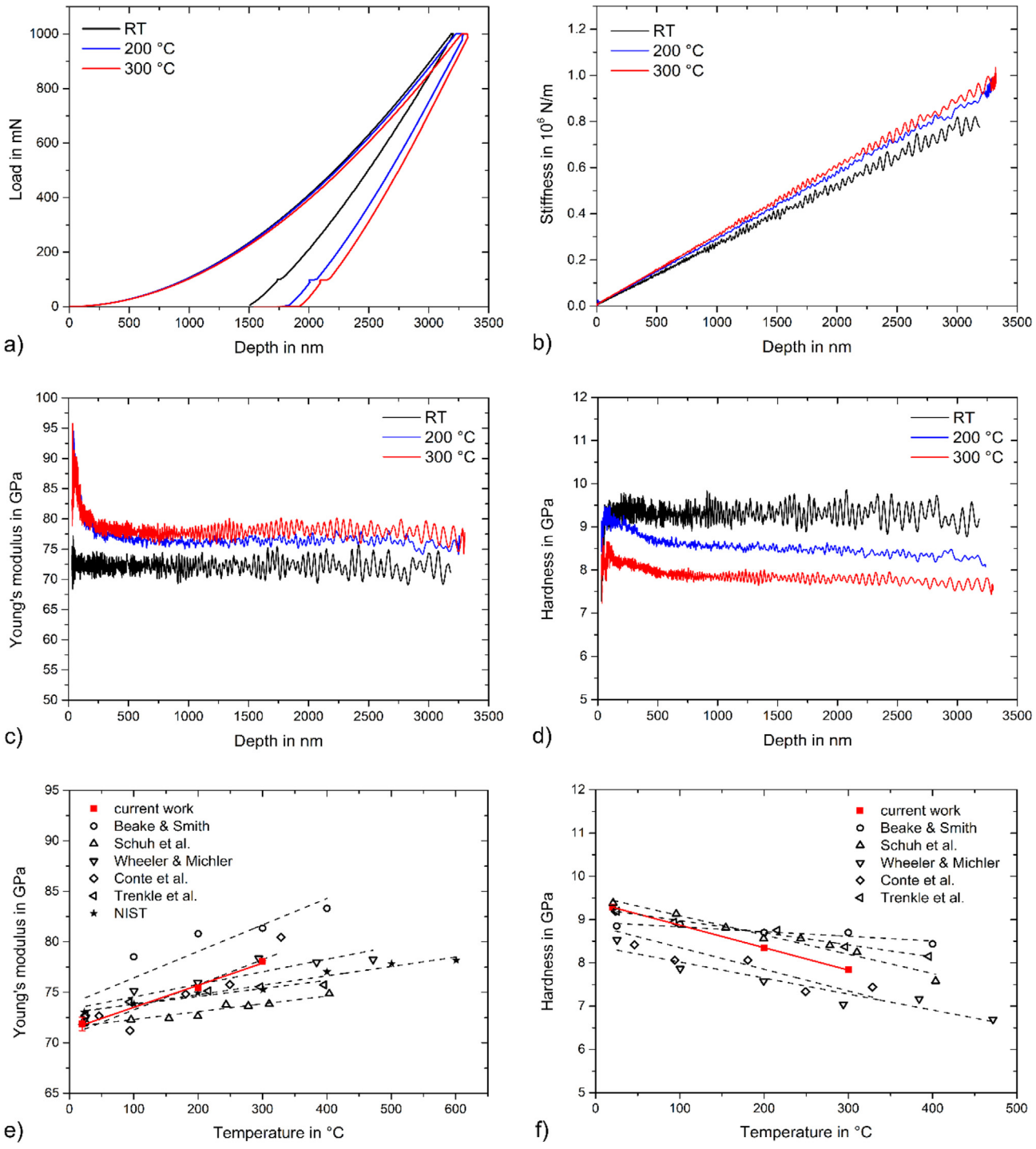

Fig. 5. a) Temperature dependent load displacement curve, b) contact stiffness vs. depth, c) Young's modulus vs. depth, d) hardness vs. depth, e) Young's modulus vs. temperature and d) hardness vs. temperature of fused silica. Literature data taken from [2,33,43,44,48,49].

from $1.276 \cdot 10^6\ ^N/_m$ at RT to $1.136 \cdot 10^6\ ^N/_m$ at 300 °C and as such nearly independent of temperature.

3.3. Molybdenum

Ultra-high temperature nanoindentation experiments on a mirror finished, commercially pure (99,95%, ASTM-B-387 Type 361), polycrystalline Mo sample were carried out using an ultra-high temperature sapphire Berkovich tip (Synton MDP). More detailed information on the tips used is given in the Appendix A.3. All tests were carried out in batch mode applying the CSM test protocol as described above. Additional RT tests on fused silica were done between each test temperature to calibrate the tip area function according to the procedure developed by Oliver and Pharr [36]. The influence of thermal expansion of the tip on the tip area function can be neglected as it is already discussed in literature [2,27].

A temperature dependent Young's modulus of sapphire as well as a temperature dependent Poisson's ratio of molybdenum was used for the analysis [27,50]. The Poisson's ration of Sapphire ($\nu_{Sap} = 0.24$)

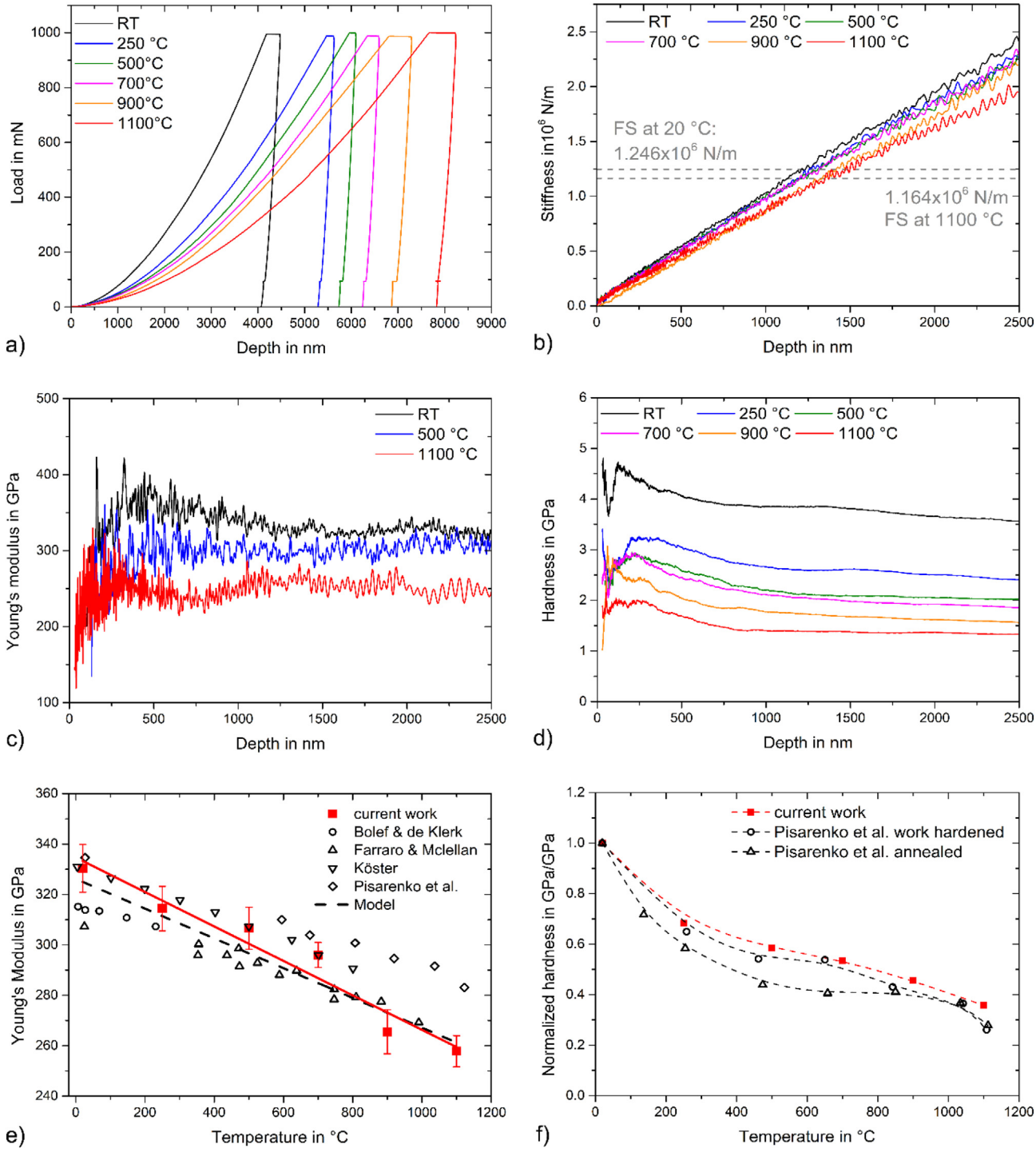

Fig. 6. a) Temperature dependent load displacement curve, b) contact stiffness vs. depth, c) Young's modulus vs. depth, d) hardness vs. depth, e) Young's modulus vs. temperature and d) hardness vs. temperature of molybdenum [51–53].

was assumed to be constant and T independent [27]. The frame stiffness was adjusted in order to get a depth independent Young's modulus. Therefore, the frame stiffness was reduced by about 6.6% from $1.246 \cdot 10^6\,{}^{N}/_{m}$ at RT to $1.164 \cdot 10^6\,{}^{N}/_{m}$ at 1100 °C (Fig. 8b). The actuator temperature was decreasing to 15.4 °C by testing at 1100 °C.

Representative, temperature dependent load-displacement curves as well as the temperature dependent stiffness data are plotted in Fig. 6a and b. The contact stiffness is slightly decreasing with increasing temperature. The stiffness follows a linear relationship for all T and depth ranges, except for the measurements at 1100 °C.

For this reason, were only data up to an indentation depth of max. 1500 nm analyzed. At this indentation depth the contact stiffness is similar to the frame stiffness of the system. At higher indentation depths, the frame compliance is larger than the contact compliance, which leads to increasing inaccuracy when determining Young's modulus, penetration depth and thus hardness. The modulus and hardness data as a function of indentation depth is plotted for several temperatures in Fig. 6c and d.

The comparison of measured hardness and Young's modulus data with literature data shown in Fig. 6e and f. Literature data for hardness were measured with a micro hardness tester, while the Young's modulus was determined by pulse-echo methods. Additionally, the Young's modulus was calculated according to the following model [54]:

$$E(T) = E(0\,K) \cdot \left(1 - 0.5\frac{T}{T_m}\right) \tag{11}$$

with E (0 K), Young's modulus at 0 K and melting temperature T_m. The fit is normalized to a room temperature modulus of 325 GPa [55].

Young's modulus data are fitting very well to the data determined by pulse-echo methods and the model, even at a temperature of 1100 °C. The good consistency of measured and literature Young's modulus data indicates the correct determination of the projected contact area and thus of the measured hardness values. The temperature dependence of H matches nicely the literature data.

3.4. Single crystalline nickel

SRJ and SLH tests were performed on SX Ni as described above. All tests were performed with UHT sapphire Berkovich tips (Synton MDP). A temperature dependent tip modulus was used for the analysis, the Poisson's ratio of Ni was assumed to be constant [27]. The sample thermocouple was placed into the Mo sheet.

In SRJ tests, hardness values immediately before and after the strain rate jump were analyzed. An overview of test statistics and SRSs are given in Table 1. The frame stiffness of the nanoindenter was adjusted from $1.166 \cdot 10^6\,{}^{N}/_{m}$, at RT to $1.001 \cdot 10^6\,{}^{N}/_{m}$ at 1100 °C. An actuator temperature of 14.4 °C was measured at the maximum test temperature.

Table 1
Strain rate sensitivity of nickel determined with SRJ and step-load creep tests.

T in °C	SRJ tests			Creep tests		
	Number of tests	Max. drift rate in nm/s	m	Number of tests	Max. drift rate in nm/s	m
RT	6	0.065	0.001	4	0.037	0.001
499	6	0.072	0.013	4	0.095	0.010
835	5	0.069	0.027	3	0.108	0.028
1009	4	0.042	0.051	5	0.136	0.060
1100	4	0.180	0.055	2	0.767	0.098

The depth dependent hardness of the SRJ tests is plotted in Fig. 7a for different temperatures. Ni is strongly softening with temperature and mainly deforms plastic. The hardness data below 1000 nm are not representative of the material response, since strong tip rounding prevents a measurement of indentation size effects at low temperature. However, for larger depths, the hardness is nearly depth independent and only an influence of T and strain rate on the hardness is found. In Fig. 7b is the

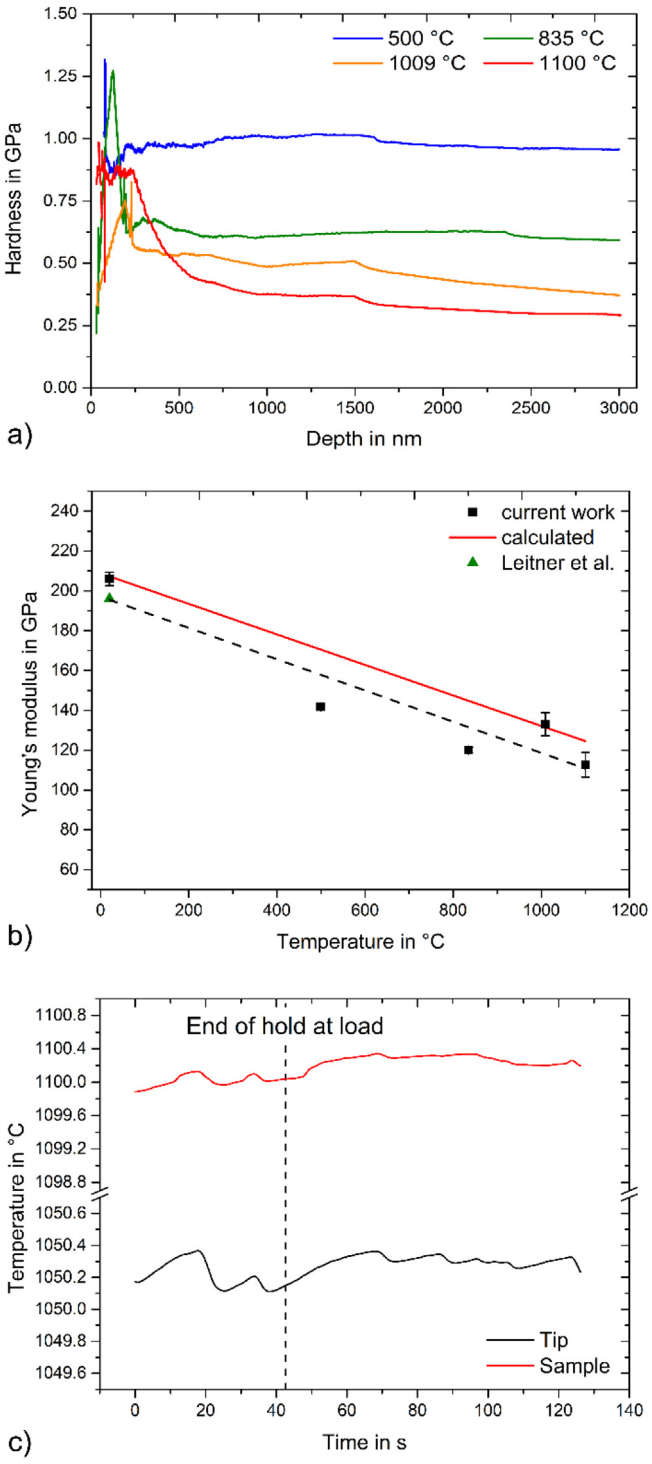

Fig. 7. a) Depth dependent hardness and b) temperature dependent modulus of SX Ni. Tip and sample temperature as a function of time during SRJ test on nickel at 1100 °C with a drift rate of 0.069 nm/s are shown in (c) [46,56,57].

temperature dependent Young's modulus plotted and compared to calculated data using Eqs. (12) and (13) [56]:

$$G(T) = 78.9(1-0.64(T-300\,K)/T_m)\;GPa\;(T_m = 1726\,K) \quad (12)$$

$$E(T) = G(T)\cdot 2(1+\nu) \quad (13)$$

with temperature T and melting temperature T_m and Poisson's ratio ν. The nanoindentation data are shifted to slightly lower values, but the temperature dependent related decrease described by the slope of the fitting lines is very similar. The temperature stability at 1100 °C (sample temperature is set temperature) is shown in Fig. 7c. The scattering is a bit higher than at lower temperatures (Fig. 4) but still good.

Fig. 8a shows the temperature dependent depth-time relationship during the performed step load and hold creep tests. The indentation strain rate as a function of hardness in Fig. 8b. High strain rates in the initial part of the tests can be achieved by applying a step load and hold the load for 1.5 s. In this first test segment is the hardness calculated by indentation depth whereas the hardness in the second part of the experiment is determined by the stiffness signal (Sneddon's hardness) using the CSM technique. The hardness values of the two test segments match very well, as can be seen from the linear relationship with the strain rate (Fig. 8b). Thus the influence of the thermal drift is low. This test protocol allows to vary the strain rate over five orders of magnitude within a single test.

The results of the SRSs determined by SRJ and creep tests are compared in Table 1. It could be demonstrated that m values determined via creep tests are in good accordance with SRJ tests. The relatively high drift rates during creep testing have a negligible influence on the results, since hardness is calculated based on the stiffness signal of the CSM measurement.

The measured hardness and strain rate were converted into uniaxial stress and strain rate using Eqs. (8) and (9) for comparison with literature data. The resulting temperature compensated uniaxial strain rate and normalized uniaxial stress data are compared with creep data from literature. This is shown in Fig. 8c. The results form SRJ und step load and hold tests show a similar behavior. Tests at 1100 °C show a small deviation, this can be attributed to the fact that a new tip was used for these tests.

The activation energy for creep can be calculated with Eq. (10) using two different strain rates. The activation energy for $\varepsilon = 0.3\;s^{-1}$ is 140 kJ/mol, whereas the activation energy in the low strain rate regime ($\varepsilon = 0.002\;s^{-1}$) 216 kJ/mol is. In literature activation energies in the range of 243–285 kJ/mol are determined. The difference to literature data can be explained by the fact that the steady state condition in the strain rate has not yet been reached, furthermore the complex stress state below the indenter.

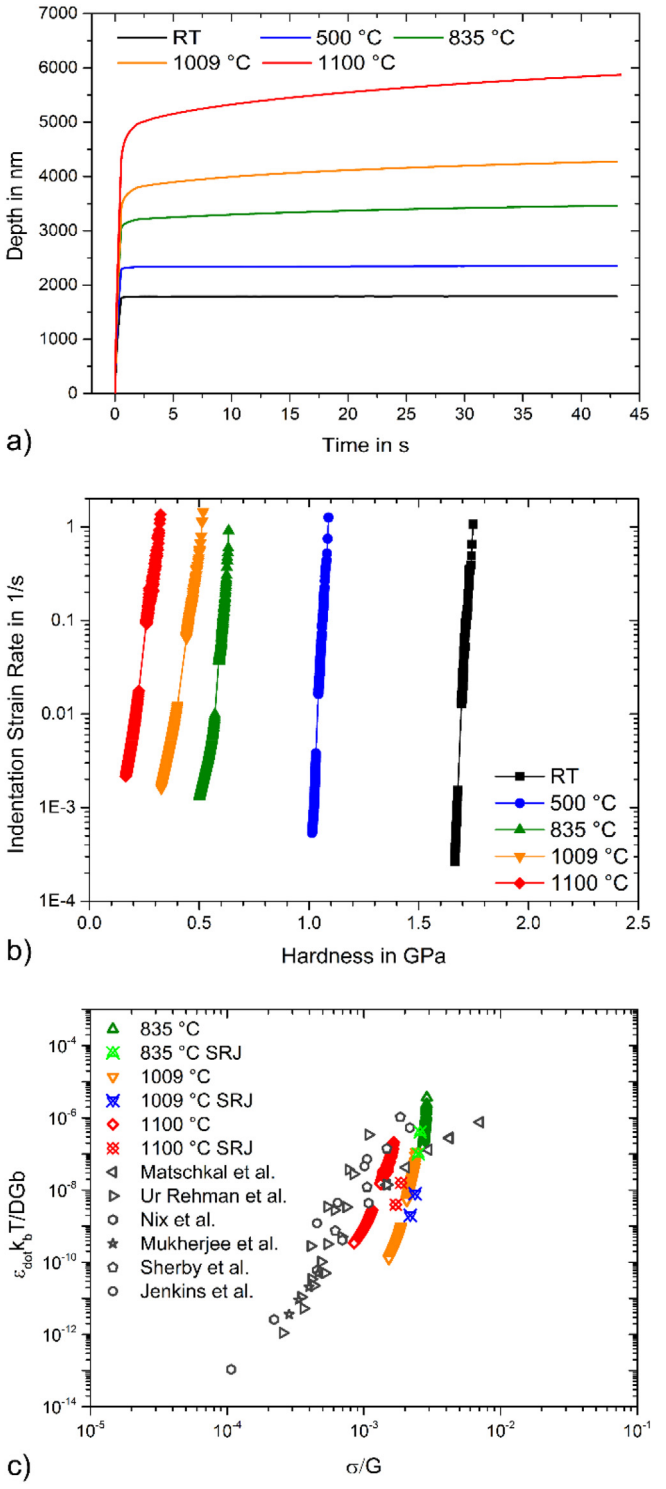

Fig. 8. A) Depth-time behavior of Ni at different temperatures using a step-load and hold test. B) Temperature dependent Indentation strain-rate as a function of hardness for nickel. C) Temperature compensated uniaxial strain rates vs. normalized uniaxial stress data [14,46,58–60].

4. Conclusion

The results of the very first nanoindentation tests using the load controlled Prometheus UHT nanoindenter manufactured by Nanomechanics/KLA has been presented. Tests with diamond and sapphire Berkovich tips at temperatures between 20 °C and 1100 °C were performed on fused silica, molybdenum and SX nickel in ⟨100⟩ orientation. The improved nanoindentation system offers for the first time the possibility to determine reliable Young's modulus and hardness data at temperatures up to 1100 °C using dynamic methods like the continuous stiffness measurement (CSM). Low drift rates even at ultra-high temperatures could be achieved by a sophisticated temperature management including multiple independent heating and cooling options. Additionally, a semi-automated temperature matching procedure has been presented.

The combination of the 1 N high load actuator and the high frame stiffness ($\geq 1\cdot 10^6\,{}^{N}/_{m}$) allows experiments to be carried out at higher indentation depths, which are less sensitive to tip wear and thermal drift. Tip and tip braze materials for operating at high temperature are still a pending issue which needs to be solved in future. Nevertheless, it could be shown that sapphire is a good tip material for testing molybdenum even at 1100 °C. Testing in nickel at high temperatures cause massive tip wear as already reported in literature [27]. The set up inside

a SEM allows in situ observations while the vacuum atmosphere minimize oxidation. It could be shown that imaging is possible up to the maximum temperature. A further improvement of the image quality will allow a good positioning or even in-situ experiments at 1100 °C in future. The temperature dependent hardness and Young's modulus data of fused silica are consistent with previous tests. The temperature control at low temperatures like 200 °C is challenging due to the low current output. Nevertheless, the excellent temperature stability at low temperature could be demonstrated. Tests at higher temperatures were performed on molybdenum and nickel. Young's modulus and hardness data correspond well with literature data. Also the temperature compensated uniaxial strain rates and normalized uniaxial stress data, as well as the determined activation energy for creep in Ni fit with literature data at least in the low strain rate regime. This demonstrated that nanoindentation experiments even under these extreme conditions give similar results as conventional uniaxial experiments.

CRediT authorship contribution statement

Christian Minnert: Investigation, Formal analysis, Data curation, Visualization, Writing - original draft. **Warren C. Oliver:** Methodology, Writing - review & editing, Resources, Supervision. **Karsten Durst:** Conceptualization, Writing - review & editing, Supervision, Resources, Funding acquisition, Project administration.

Declaration of competing interest

The authors declare no conflict of interest.

Acknowledgement

The authors would like to thank Rich Anthony and Sam Bacon for technical support during the experimental part. The authors gratefully acknowledge Deutsche Forschungsgemeinschaft (DFG) for financial support within the framework of the project “Indentation creep: New machine and test methodology development at various length scales, high temperatures and low deformation rates” (DU 424/11-1). Further financial support was gratefully provided by the Open Access Publication Fund of the Technical University of Darmstadt.

Data availability

The raw/processed data required to reproduce these findings cannot be shared at this time as the data also forms part of an ongoing study.

Appendix A

A.1. Influence of temperature on the actuator calibration

As mentioned above is the actuator temperature is slightly changing during testing at non ambient temperatures. The maximum temperature of the actuator is controlled by an active cooling of the actuator housing. Whereas the lowest actuator temperature is controlled by the cooling water temperature which has to be reduced with increasing test temperature. In consequence, the actuator temperature was decreasing with increasing test temperature from RT to 14.4 °C, the maximum actuator temperature was 23.8 °C.

In order to investigate the influence of temperature on the calibration, the actuator was cooled down to 12 °C and heated up to 25 °C using the water circuit described above. In Fig. 9, the temperature dependent phase angle (Fig. 9a), compliance (Fig. 9b) and damping (Fig. 9c) are plotted. The data are nearly constant, only for the damping a small deviation could be observed, which is however in the range of the scattering [61–64].

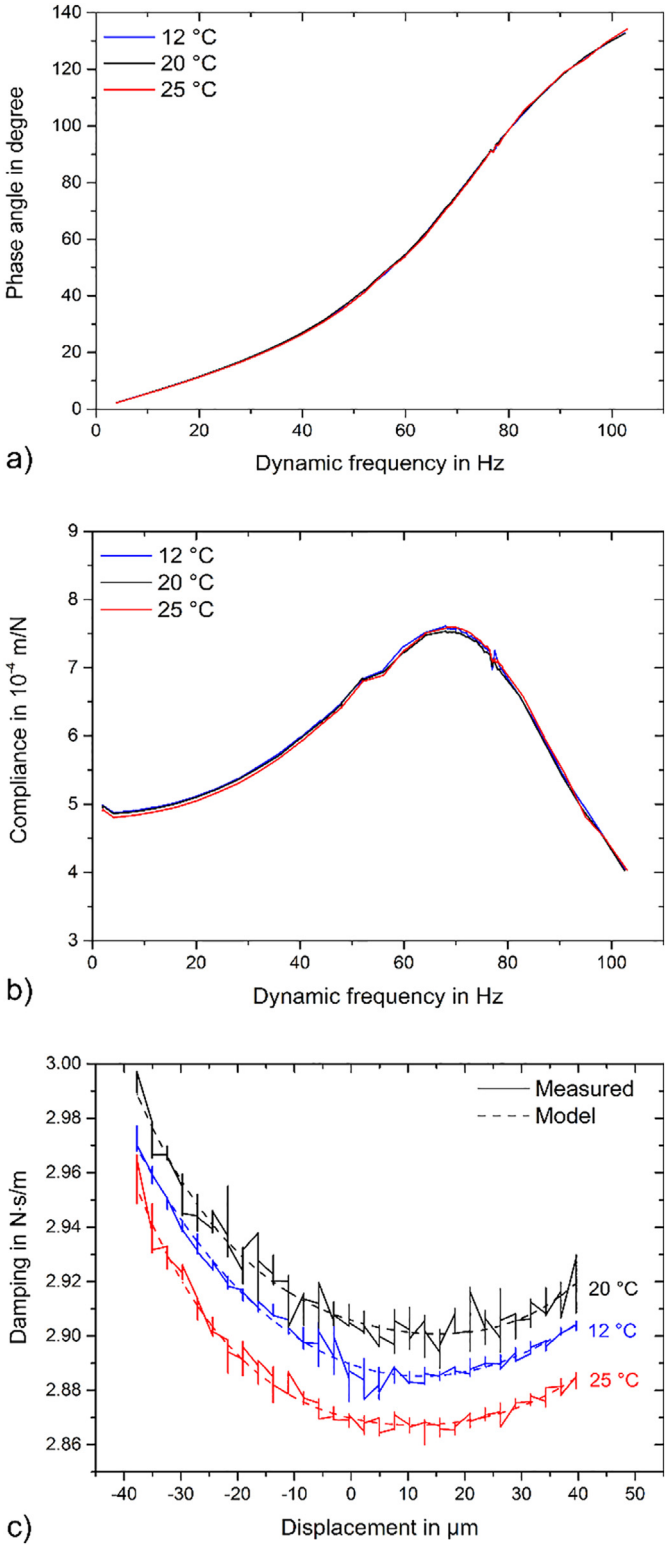

Fig. 9. Influence of temperature on calibration. A) Phase angle vs. Dynamic frequency, b) Compliance vs. Dynamic frequency and c) Damping vs. Displacement.

A.2. Semi-automated temperature matching procedure

Before starting the temperature matching process, the sample and tip are heated to the same temperature and hold there for a couple of minutes until temperatures are settled and thermal gradients caused

by fast heating (10 K/min) are minimized. During the T matching procedure, the tip is brought into contact with the sample for a few seconds using a predefined constant force e.g. 25 mN and then removed from the sample surface again (see Fig. 10a–b). This loading- unloading procedure is automatically repeated several times. The raw displacement (Fig. 10b) and the temperatures of the tip and sample are continuously recorded (Fig. 10c–d). Now, either the tip or the sample temperature has to be varied manually until the drift rate is steadily decreasing. The corresponding contact and system drift are calculated independently by the software (Fig. 10e–f).

The system drift is related to the displacement change between the individual loading cycles. This change is caused by thermal expansion or contraction of the system/gantry which affects the spacing between the tip and the sample surface. The system drift can therefore be calculated by the slope between the individual segments (overall slope) where the positive load is applied (see Fig. 10b and e). This overall displacement change will be superimposed with a displacement change due to the temperature mismatch of the contact. The tip side is more sensitive to temperature mismatches compared to the sample side due to the lower heat capacity (Fig. 10c–d). A changing tip temperature leads to a thermal expansion or contraction and thus to a change in displacement signal. The curvature of the displacement signal depends on the relative temperatures of tip and sample. Low thermal drift values result in a linear changing displacement. The change in displacement within a loading cycle (positive load applied) is related to the contact drift (Fig. 10b, f). It goes towards zero as soon as the system is in thermal equilibrium. The Influence of creep on the displacement signal will be reduced by continuously indenting at the same position.

The independent determination of system drift and contact drift allows to start the temperature setting of tip and sample already before the system/gantry is in thermal equilibrium which reduces the time for temperature adjustment significantly. In the example shown above (Fig. 10), the temperature of the sample was increased (Fig. 10d) until drift rates close to zero were reached. The difference in tip and sample temperature, here about 35 K, is mainly caused by a temperature gradient between the top and bottom side of the sample. The thermocouple for measuring the sample temperature is placed in the Mo sheet close to the heater and is therefore not measuring the exact surface temperature of the sample. The surface temperature of the sample is lower due to radiation and heat transfer through the tungsten wires used for sample clamping. The small change in tip temperature (Fig. 10c) while loading and unloading is also effected by the relatively large alterations in displacement which causes different conditions in terms of heat transfer.

A.3. Indenter tips

In this work a standard diamond Berkovich tip from MicroStar as well as three ultra-high temperature sapphire Berkovich tips manufactured by Synton MDP were used. All tests from RT to 300 °C, on fused silica were performed with the diamond tip. The maximum operational temperature of this tip is limited by the epoxy glue used to fix the tip in the holder. Molybdenum and Nickel were tested with the UHT sapphire tips. These tips were brazed at temperatures of 1500–1600 °C in a high vacuum environment and can therefore be operated up to 1100 °C.

The contact areas of the sapphire tips are plotted as a function of depth and temperature in Fig. 11. All tip area functions were determined at RT using fused silica as reference material. The sapphire tip show no excessive tip wear during testing Mo (see Fig. 11a) which is consistent with previous tests reported in literature [27].

Testing nickel at temperatures above 500 °C leads to a significantly changing tip area function (Fig. 11b). After testing at 1009 °C a huge change in the area function was observed, caused by tip wear or material adhesion to the tip. Therefore, two different tips were used in this study for testing Ni. The sapphire tips were sticking in the nickel sample at these extreme temperatures, high forces have to be applied to retract the tip from the sample surface.

It could also be demonstrated that the high temperature tips are able to withstand these ultra-high temperatures. The necessity for new tip materials for future long term creep experiments on nickel and nickel based alloys has been demonstrated.

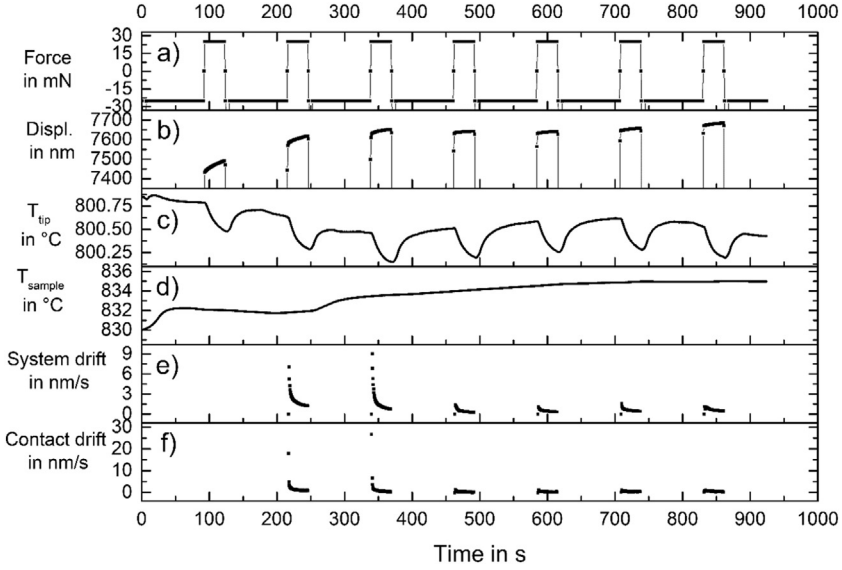

Fig. 10. Semi-automated procedure for temperature adjustment, shown exemplarily for Ni at 800 °C. A) Applied force, b) displacement, c) tip temperature, d) sample temperature, e) system drift and f) contact drift as a function of time.

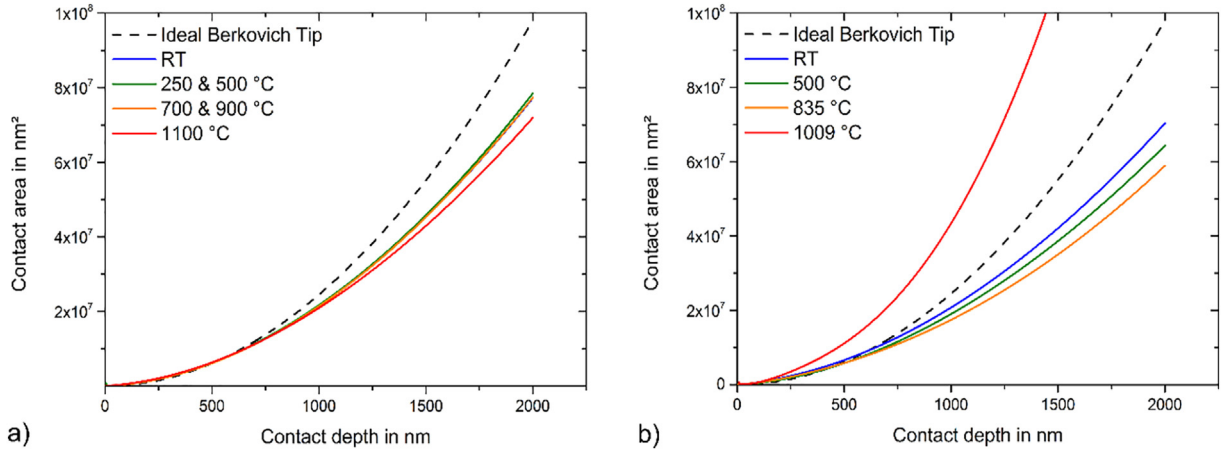

Fig. 11. Evolution of contact area as a function of contact depth and test temperature during indenting a) molybdenum and b) nickel with a sapphire Berkovich tip.

References

[1] J.M. Wheeler, et al., High temperature nanoindentation: the state of the art and future challenges, Curr. Opinion Solid State Mater. Sci. 19 (6) (2015) 354–366.
[2] C.A. Schuh, C.E. Packard, A.C. Lund, Nanoindentation and contact-mode imaging at high temperatures, J. Mater. Res. 21 (3) (2006) 725–736.
[3] V. Maier, et al., Nanoindentation strain-rate jump tests for determining the local strain-rate sensitivity in nanocrystalline Ni and ultrafine-grained Al, J. Mater. Res. 26 (11) (2011) 1421–1430.
[4] J. Ast, et al., A review of experimental approaches to fracture toughness evaluation at the micro-scale, Mater. Des. 173 (2019), 107762.
[5] V. Maier, et al., An improved long-term nanoindentation creep testing approach for studying the local deformation processes in nanocrystalline metals at room and elevated temperatures, J. Mater. Res. 28 (9) (2013) 1177–1188.
[6] P. Cavaliere, Cyclic deformation of ultra-fine and nanocrystalline metals through nanoindentation: similarities with crack propagation, Procedia Engineering 2 (1) (2010) 213–222.
[7] Y.-C. Huang, S.-Y. Chang, C.-H. Chang, Effect of residual stresses on mechanical properties and interface adhesion strength of SiN thin films, Thin Solid Films 517 (17) (2009) 4857–4861.
[8] A. Saini, T. Pollock, High-temperature materials increase efficiency of gas power plants, MRS Bull. 37 (6) (2012) 550–551.
[9] R. Webler, et al., Evolution of microstructure and mechanical properties of coated co-base superalloys during heat treatment and thermal exposure, Mater. Sci. Eng. A 628 (2015) 374–381.
[10] R. Darolia, Development of strong, oxidation and corrosion resistant nickel-based superalloys: critical review of challenges, progress and prospects, Int. Mater. Rev. 64 (6) (2019) 355–380.
[11] H. Long, et al., Microstructural and compositional design of Ni-based single crystalline superalloys — a review, J. Alloys Compd. 743 (2018) 203–220.
[12] D. Bürger, et al., Creep properties of single crystal Ni-base superalloys (SX): a comparison between conventionally cast and additive manufactured CMSX-4 materials, Mater. Sci. Eng. A 762 (2019) 138098.
[13] N. Volz, et al., Thermophysical and mechanical properties of advanced single crystalline co-base Superalloys, Metall. Mater. Trans. A 49 (9) (2018) 4099–4109.
[14] D. Matschkal-Amberger, et al., New flat-punch indentation creep testing approach for characterizing the local creep properties at high temperatures, Mater. Des. 183 (2019), 108090.
[15] K. Durst, M. Göken, Micromechanical characterisation of the influence of rhenium on the mechanical properties in nickel-base superalloys, Mater. Sci. Eng. A 387–389 (2004) 312–316.
[16] A. Barnoush, et al., In situ small-scale mechanical testing under extreme environments, MRS Bull. 44 (6) (2019) 471–477.
[17] J. Kappacher, et al., Thermally activated deformation mechanisms and solid solution softening in W-re alloys investigated via high temperature nanoindentation, Mater. Des. 189 (2020), 108499.
[18] K. Durst, V. Maier, Dynamic nanoindentation testing for studying thermally activated processes from single to nanocrystalline metals, Curr. Opinion Solid State Mater. Sci. 19 (6) (2015) 340–353.
[19] J.M. Wheeler, et al., Activation parameters for deformation of ultrafine-grained aluminium as determined by indentation strain rate jumps at elevated temperature, Mater. Sci. Eng. A 585 (2013) 108–113.
[20] P.S. Phani, W. Oliver, G. Pharr, On the measurement of power law creep parameters from instrumented indentation, JOM 69 (11) (2017) 2229–2236.
[21] P.S. Phani, W. Oliver, A direct comparison of high temperature nanoindentation creep and uniaxial creep measurements for commercial purity aluminum, Acta Mater. 111 (2016) 31–38.
[22] M. Chen, et al., Size-dependent plasticity and activation parameters of lithographically-produced silicon micropillars, Mater. Des. 189 (2020), 108506.
[23] G. Mohanty, et al., Elevated temperature, strain rate jump microcompression of nanocrystalline nickel, Philos. Mag. 95 (16–18) (2015) 1878–1895.
[24] J. Wehrs, et al., Comparison of in situ micromechanical strain-rate sensitivity measurement techniques, JOM 67 (8) (2015) 1684–1693.
[25] C. Su, et al., Measurement of power-law creep parameters by instrumented indentation methods, Journal of the Mechanics and Physics of Solids 61 (2) (2013) 517–536.
[26] G. Guillonneau, et al., Nanomechanical testing at high strain rates: new instrumentation for nanoindentation and microcompression, Mater. Des. 148 (2018) 39–48.
[27] J. Wheeler, J. Michler, Invited article: indenter materials for high temperature nanoindentation, Rev. Sci. Instrum. 84 (10) (2013), 101301.
[28] Y. Li, et al., In situ measurement of oxidation evolution at elevated temperature by nanoindentation, Scr. Mater. 103 (2015) 61–64.
[29] Y. Li, et al., Effects of creep and oxidation on reduced modulus in high-temperature nanoindentation, Mater. Sci. Eng. A 678 (2016) 65–71.
[30] Y. Li, et al., Microstructure evolution of FeNiCr alloy induced by stress-oxidation coupling using high temperature nanoindentation, Corros. Sci. 135 (2018) 192–196.
[31] J. Langevoort, et al., On the oxide formation on stainless steels AISI 304 and incoloy 800H investigated with XPS, Appl. Surf. Sci. 28 (2) (1987) 167–179.
[32] J.S.K.L. Gibson, et al., On extracting mechanical properties from nanoindentation at temperatures up to 1000 °C, Extreme Mechanics Letters 17 (2017) 43–49.
[33] J.C. Trenkle, C.E. Packard, C.A. Schuh, Hot nanoindentation in inert environments, Rev. Sci. Instrum. 81 (7) (2010), 073901.
[34] B.D. Beake, et al., Temperature dependence of strain rate sensitivity, indentation size effects and pile-up in polycrystalline tungsten from 25 to 950° C, Mater. Des. 156 (2018) 278–286.
[35] I.N. Sneddon, The relation between load and penetration in the axisymmetric Boussinesq problem for a punch of arbitrary profile, Int. J. Eng. Sci. 3 (1) (1965) 47–57.
[36] W.C. Oliver, G.M. Pharr, An improved technique for determining hardness and elastic modulus using load and displacement sensing indentation experiments, J. Mater. Res. 7 (6) (1992) 1564–1583.
[37] M.J. Mayo, W.D. Nix, A micro-indentation study of superplasticity in Pb, Sn, and Sn-38 wt% Pb, Acta Metall. 36 (8) (1988) 2183–2192.
[38] D.L. Joslin, W.C. Oliver, A new method for analyzing data from continuous depth-sensing microindentation tests, J. Mater. Res. 5 (1) (1990) 123–126.
[39] B.N. Lucas, W.C. Oliver, Indentation power-law creep of high-purity indium, Metall. Mater. Trans. A 30 (3) (1999) 601–610.
[40] O. Prach, et al., A new nanoindentation creep technique using constant contact pressure, J. Mater. Res. 34 (14) (2019) 2492–2500.
[41] P. Sudharshan Phani, W.C. Oliver, Ultra high strain rate Nanoindentation testing, Materials 10 (6) (2017) 663.
[42] J. Wheeler, P. Brodard, J. Michler, Elevated temperature, in situ indentation with calibrated contact temperatures, Philos. Mag. 92 (25–27) (2012) 3128–3141.
[43] J.M. Wheeler, J. Michler, Elevated temperature, nano-mechanical testing in situ in the scanning electron microscope, Rev. Sci. Instrum. 84 (4) (2013), 045103.
[44] M. Conte, et al., Novel high temperature vacuum nanoindentation system with active surface referencing and non-contact heating for measurements up to 800° C, Rev. Sci. Instrum. 90 (4) (2019) 45105.
[45] G. Feng, A. Ngan, Effects of creep and thermal drift on modulus measurement using depth-sensing indentation, J. Mater. Res. 17 (3) (2002) 660–668.
[46] H. ur Rehman, et al., On the temperature dependent strengthening of nickel by transition metal solutes, Acta Mater. 137 (2017) 54–63.
[47] A. Sato, et al., On the mechanical behavior of a new single-crystal Superalloy for industrial gas turbine applications, Metall. Mater. Trans. A 43 (7) (2012) 2302–2315.
[48] B.D. Beake, J.F. Smith, High-temperature nanoindentation testing of fused silica and other materials, Philosophical Magazine A 82 (10) (2002) 2179–2186.
[49] R.G. Munro, NIST Interagency/Internal Report No. 6853, 2002.
[50] H. Su, et al., Temperature-dependent Modulus of metals based on lattice vibration theory, J. Appl. Mech. 81 (4) (2013) 41017–041017–4.
[51] R. Farraro, R.B. Mclellan, Temperature dependence of the Young's modulus and shear modulus of pure nickel, platinum, and molybdenum, Metall. Trans. A. 8 (10) (1977) 1563–1565.

[52] G. Pisarenko, V. Borisenko, Y.A. Kashtalyan, The effect of temperature on the hardness and modulus of elasticity of tungsten and molybdenum (20–2700‡), Soviet Powder Metallurgy and Metal Ceramics 1 (5) (1964) 371–374.
[53] D.I. Bolef, J. De Klerk, Elastic constants of single-crystal Mo and W between 77 and 500 K, J. Appl. Phys. 33 (7) (1962) 2311–2314.
[54] J. Roesler, H. Harders, M. Baeker, Mechanical Behaviour of Engineering Materials, Springer, 2007.
[55] F. Caradelli, Materials Handbook, second edition Springer, 2008.
[56] Y. Li, et al., Deformation kinetics of nanocrystalline nickel, Acta Mater. 55 (17) (2007) 5708–5717.
[57] A. Leitner, V. Maier-Kiener, D. Kiener, Dynamic nanoindentation testing: is there an influence on a material's hardness? Materials Research Letters 5 (7) (2017) 486–493.
[58] W.D. Nix, B. Ilschner, Mechanisms controlling creep of single phase metals and alloys, in: P. Haasen, V. Gerold, G. Kostorz (Eds.), Strength of Metals and Alloys, Pergamon 1979, pp. 1503–1530.
[59] A.K. Mukherjee, J.E. Bird, J.E. Dorn, Experimental Correlations for High-Temperature Creep, 1968.
[60] O.D. Sherby, P.M. Burke, Mechanical behavior of crystalline solids at elevated temperature, Prog. Mater. Sci. 13 (1968) 323–390.
[61] J. Weertman, P. Shahinian, Creep of polycrystalline nickel, JOM 8 (10) (1956) 1223–1226.
[62] G.J. Richardson, C.M. Sellars, W.J.M. Tegart, Recrystallization during creep of nickel, Acta Metall. 14 (10) (1966) 1225–1236.
[63] S. Karashima, H. Oikawa, T. Motomiya, Steady-state creep characteristics of polycrystalline nickel in the temperature range 500° to 1000°C, Trans. Jpn. Inst. Metals 10 (3) (1969) 205–209.
[64] H. Oikawa, T. Kato, S. Karashima, Activation parameters of high-temperature creep in nickel, and in Ni-9.5at% Cr and Ni-10.3at% W alloys, Trans. Jpn. Inst. Metals 14 (5) (1973) 389–395.